Journal of Materials Chemistry A

ROYAL SOCIETY OF CHEMISTRY

PAPER

View Article Online
View Journal | View Issue

Cite this: J. Mater. Chem. A, 2025, 13, 13262

In situ transformation of a liquid electrolyte into a solid polymer electrolyte: influence of TMSP in a layered $LiNi_{0.82}Mn_{0.12}Al_{0.06}O_2$ cathode†

Sreekumar Sreedeep,[a] Yun-Sung Lee *[b] and Vanchiappan Aravindan *[a]

Received 9th December 2024
Accepted 20th March 2025

DOI: 10.1039/d4ta08731c

rsc.li/materials-a

Herein, we successfully demonstrated a thermal polymerization technique for the *in situ* transformation of a commercial liquid electrolyte into a gel-solid polymer electrolyte (G-SPE). In addition, an attempt has been made to improve the interfacial contact and electrolyte stability by introducing a film-forming additive, tris(trimethylsilyl)phosphate (TMSP), and its influence on the electrochemical stability has been studied by varying its concentration and is denoted as G-SPE_TMSP (1–5 wt%). The electrochemical studies reveal enhanced ionic conductivity and transference number, when the TMSP concentration is increased from 1 to 5 wt%. The unique behavior originated from the increase in thickness of the cathode electrolyte interphase (CEI) layer formation. To demonstrate the feasibility of using G-SPE_TMSP in practical cells, a Li-battery has been made with $LiNi_{0.82}Mn_{0.12}Al_{0.06}O_2$ (NMA) as the cathode and Li metal as the anode. The galvanostatic charge–discharge studies exhibit an enhancement in the electrochemical performance as the concentration of TMSP is increased from 1 to 5 wt% due to an increase in the stability of the CEI–gel interface. The *in operando* analysis shows the absence of phase transition. Moreover, post-analysis of the electrode and electrolyte reveals the absence of parasitic side reactions between the electrode and electrolyte. Therefore, the G-SPE promotes excellent cycle stability and coulombic efficiency in the cell assembly.

Introduction

Fossil fuels are the primary energy source that revolutionized the research and development in the modern world.[1,2] They have become an integral part of society, and a life without these resources has become impossible. However, the rise in the demand for these resources has eventually led to their depletion from the Earth's crust. Also, the emission of greenhouse gases, such as NO, CO, *etc.*, by the combustion of fossil fuels accounts for a major share of global warming.[2–8] Although renewable energy, due to its abundance and eco-friendly nature, is an alternative to fossil fuels, its transient and inconsistent nature are their major setbacks. To mitigate these issues, the development of energy storage devices, especially electrochemical energy storage devices such as batteries, is gaining a lot of interest. Li-ion batteries (LIBs) have gained attention as a promising battery technology owing to their high energy density, excellent gravimetric and volumetric capacity, and lightweight. The wide range of applications of LIBs, especially in electric vehicles (EVs), has led to their progressive development.[9–11] Among the various components, the electrolyte plays a prominent role in enhancing the stability and electrochemical performance of batteries. However, the development of non-aqueous electrolytes is hindered due to their poor electrochemical stability window (for carbonate-based electrolytes ~4.3 V *vs.* Li), which results in parasitic side reactions, leading to the dissolution of active materials from the electrode. In addition, it also promotes dendritic growth, which results in safety issues.[12–17] However, solid electrolytes (SEs), owing to their large stability window and ability to prevent dendrite formation, are promising compared to liquid electrolytes. The SEs can be categorized into inorganic (garnets, sulfides, and lithium phosphorus oxynitride (LIPON))-[18,19] and polymer-based SEs (SPEs).[19–21] Although inorganic SEs possess high ionic conductivity (sulfide ~10^{-2} S cm^{-1}; garnet 10^{-3} S cm^{-1}), the high interfacial resistance due to poor electrode–electrolyte contact and brittle nature are the major setbacks. In contrast, SPEs, owing to their flexible and amorphous nature, are a better alternative to inorganic SEs. However, SPEs possess several setbacks due to poor electrode–electrolyte contact and low ionic conductivity (10^{-5} to 10^{-7} S cm^{-1}).[22]

To mitigate these setbacks, various strategies have been implemented, among which the addition of functional fillers, employing a suitable polymer matrix, and improving the interfacial contact between the electrode and SEs are found to

[a]Department of Chemistry, Indian Institute of Science Education and Research (IISER), Tirupati-517619, Andhra Pradesh, India. E-mail: aravind.van@gmail.com
[b]School of Chemical Engineering, Chonnam National University, Gwang-ju, 61186, Republic of Korea. E-mail: leeys@chonnam.ac.kr

† Electronic supplementary information (ESI) available. See DOI: https://doi.org/10.1039/d4ta08731c

be more effective. The fillers play a crucial role in improving the ionic conductivity by the formation of suitable channels for the diffusion of ions in the SPE. In addition, it also enhances the mechanical and thermal stability of the SPE. The fillers can be classified as inorganic (BN, SiO_2, and TiO_2)- and organic (MOF, COF, cellulose, and ionic liquid)-based fillers.[23–25] The fillers facilitate Li-ion conductivity by preventing the crystallization of the polymer and maintaining its amorphous nature. In addition, it also reduces the interfacial resistance by improving the contact between the electrode and the electrolyte. Employing a suitable polymer matrix is an effective strategy to improve the mechanical strength of the SPE. The commonly employed polymer matrix for SPEs includes poly(ethylene oxide) (PEO), succinonitrile (SN), and poly(methyl methacrylate) (PMMA). However, the crystallization of PEO at room temperature, leading to poor ionic conductivity and the parasitic side reactions of SN with Li metal and graphite forming an unstable solid electrolyte interphase (SEI), has hampered the development of SPEs. In addition, the rigorous solution casting method for the preparation of PMMA-based SPEs makes them less economical and sustainable.[22,26,27] However, poly(vinylidene fluoride)-*co*-hexafluoropropylene (PVDF-HFP) with a high dielectric constant, excellent oxidation stability, and high thermal stability is an effective polymer alternative for SPEs. Also, the HFP co-polymer provides a conductive channel for efficient Li-ion diffusion.[28]

Although the aforementioned strategies are effective in enhancing the electrolyte properties, none are effective in mitigating the poor electrode–electrolyte contact, causing high interfacial resistance. Hence, improving the contact between the electrode and SPEs is essential to mitigate the high interfacial resistance. Among the various strategies that has been implemented so far, *in situ* polymerization is found to be effective in improving the contact between the electrode and the SPE.[29] In this process, the polymerizable small molecules in the electrolyte will get converted into a gel in the presence of an initiator, forming a stable and compatible interface between the electrode and the SPE. In addition, the *in situ* polymerization also increases the oxidation stability of the SPE by increasing the HOMO–LUMO energy gap, thereby increasing the electrolyte stability window of the SPE.[29] Moreover, the stable gel interface between the electrode and SPE will prevent the transition metal dissolution, which enhances the cycle stability and coulombic efficiency. Zhou *et al.*[29] have used *in situ* polymerization for the formation of an interlayer consisting of SN, lithium tris(trifluoromethane) sulfonylimide (LiTFSI), lithium bis(oxalate)borate (LiBOB), and tri(propyleneglycol)diacrylate at the interphase of $Li_{1.5}Al_{0.5}Ge_{1.5}(PO_4)_3$ (LAGP) and the cathode using $C_8H_{12}N_4$ as the initiator. The as-formed interphase exhibited enhanced electrochemical stability by preventing the electrolyte decomposition at a high potential of 4.8 V *vs.* Li. In addition, the $Li/LiNi_{0.8}Co_{0.15}Al_{0.05}O_2$ cell has shown better capacity retention of 80% after cycling up to 100 cycles. Also, Chen *et al.*[24] developed a strategy of UV-induced polymerization for the preparation of single-ion conducting polymer electrolytes, which has shown a wide electrochemical stability window of ~5.3 V *vs.* Li.

Taking into account all these strategies, herein, we are attempting to improve the interfacial stability of the gel-solid polymer electrolyte (G-SPE) by employing a phosphorus-based electrolyte additive, *i.e.*, tris(trimethylsilyl)phosphate (TMSP).[30,31] Also, the effect of TMSP on the stability of the gel–polymer interface has been studied by varying its concentration from 1 to 5 wt%. In addition, the electrochemical studies of the G-SPE have been carried out by combining the G-SPE with a Co-free, Ni-rich $LiNi_{0.82}Mn_{0.12}Al_{0.06}O_2$ (NMA) cathode. Also, *in operando* XRD of NMA with the G-SPE was performed to understand the process of polymerization and the evolution of the dynamic phase. Moreover, the temperature study was carried out at different temperatures, from −10 to 70 °C, to understand their feasibility under different climatic conditions.

Experimental section

Preparation of gel-solid polymer electrolyte

For the preparation of the SPE film, the polymer PVDF-HFP (Sigma Aldrich, $M_w \sim 400\,000$) was dissolved in a 1 : 1 mixture of acetone (Thermo Fisher) and tetrahydrofuran. To the above mixture, 1.5 wt% of BN (Sigma Aldrich, ~1 μm, 98%) was added and stirred overnight for the homogeneous mixing of the solution. The slurry was then coated onto a glass plate, which was then kept aside for evaporation of the solvent. The as-obtained film was cut into circular shapes using a separator cutter and kept for drying in a vacuum oven at 75 °C. Now, the dried film was inserted into the glovebox and immersed in the liquid electrolyte for 24 hours for the infiltration of the electrolyte.

The preparation of the liquid electrolyte was carried out in the glovebox. For the preparation of the liquid electrolyte, different concentrations of TMSP ranging from 1 to 5 wt% were dissolved in the electrolyte 1 M $LiPF_6$ in ethylene carbonate (EC) and dimethyl carbonate (DMC) (1 : 1 weight ratio, LIPASTE, Tomiyama) along with azobisisobutyronitrile (AIBN, Sigma-Aldrich) as the polymerization initiator. The liquid electrolyte was stirred overnight in the glovebox for the proper dissolution and homogeneous mixing of the solution. The SPE film was soaked so that the liquid electrolyte could infiltrate the film. Then, the SPE film was heat-treated for the polymerization to occur. The as-obtained electrolyte was the gel-solid polymer electrolyte (G-SPE_TMSP (1–5 wt%)).

Synthesis and electrode preparation of NMA

NMA was synthesized using a coprecipitation method. Stoichiometric amounts of $NiSO_4 \cdot 6H_2O$ (Sigma-Aldrich, ≥98%), $MnSO_4 \cdot H_2O$ (Sigma-Aldrich, ≥99%), and $Al(NO_3)_3 \cdot 9H_2O$ (Sigma-Aldrich, 99.99%) were weighed and dissolved in a specific volume of deionized water. An aqueous solution of KOH (Sigma-Aldrich, 99.99%) was added dropwise to the solution for the precipitation to commence. The as-obtained solution was kept aside for the precipitate to settle down, washed with both deionized water and ethanol, and then dried. Then, a stoichiometric amount of Li_2CO_3 (Sigma-Aldrich) was mixed

with the dried sample and calcined at 800 °C for 12 h to obtain the final product.

For the electrode preparation, all the materials, including the active material (NMA), conductive carbon (acetylene black), and binder (TAB, teflonized acetylene black-2), were taken in a weight ratio of 10 : 2 : 2 (in mg) and were mixed properly with ethanol as a medium. The mixing was done until a free-standing film was obtained, which was then pressed onto a stainless-steel mesh (14 mm, Goodfellow, UK) using a pellet presser and a hydraulic press (Specac, UK). Moisture was removed from the electrodes by keeping them in a vacuum oven at a temperature of 75 °C. Then, the electrodes were inserted into the glovebox for cell fabrication.

Cell fabrication

The coin cells were fabricated inside an Ar-filled glovebox with O_2 < 0.1 ppm and H_2O < 0.1 ppm. For coin-cell fabrication, a CR2016 coin-cell setup was employed. In contrast to the normal cell fabrication, the G-SPE was employed as a separator-cum-electrolyte. The fabricated cell was subjected to thermal treatment in a vacuum oven at 75 °C for 1 h for the infiltrated liquid electrolyte to polymerize, forming a gel interphase.

The determination of the transference number and stability of the G-SPE (TMSP: 1–5 wt%) was carried out using the non-blocking symmetric cell analysis with the configuration Li/G-SPE_TMSP (1–5 wt%)/Li. Also, the activation energy and ionic conductivity were evaluated using the blocking symmetric cell analysis with the configuration stainless-steel spacer (SS)/G-SPE_TMSP (1–5 wt%)/SS. The asymmetric cell was fabricated with the configuration SS/G-SPE_TMSP (1–5 wt%)/Li for linear-sweep voltammetry (LSV) measurements to determine the oxidation stability of the electrolyte.

The asymmetric cell was fabricated by the preparation of a free-standing film by combining 10 mg of NMA, 2 mg of conductive carbon (acetylene black), and 2 mg of binder (teflonized acetylene black, TAB-2) using ethanol as a medium. The as-prepared film was then pressed on a 14 mm stainless steel mesh (Goodfellow), followed by cell fabrication against Li as the anode in a glovebox. The fabricated cell was then subjected to galvanostatic charge–discharge analysis within a potential window of 2.8–4.4 V *vs.* Li. The thickness of the Li foil used for the preparation of half-cells was 0.75 mm. Electrochemical characterization was performed in an electrochemical workstation (Solatron) and a battery tester (BioLogic, France). EIS analysis was carried out with a coin cell of the configuration NMA/G-SPE_TMSP (1–5 wt%)/Li using a battery tester (BioLogic, France) within a frequency range of 10 kHz to 0.1 Hz and a voltage amplitude of 10 mV.

Material characterization

The XRD analysis of the film, the cathode, and the electrodes was carried out on an X-ray diffractometer (Rigaku, SmartLab 9 kW) with monochromatic Cu Kα radiation (λ = 1.5406 Å) at a scan rate of 0.2° min^{-1} within 2θ values ranging from 10 to 90° to determine the structure and phase of the sample. In addition, *in situ* XRD analysis of NMA with G-SPE (TMSP-3 wt%) was carried out to understand the dynamic phase evolution accompanying the charge–discharge. The functional group analysis of G-SPE_TMSP (1–5 wt%) was carried out using IR-spectral analysis. The post-analysis of the G-SPE and the electrodes was carried out using FE-SEM (ZEISS) and XRD to understand the elemental composition and morphology before and after cycling. In addition, the amount of electrolyte infiltrated into the film was quantified by soaking the film in the electrolyte for 24 h, and it was calculated using the following formula:

$$\%\ \text{electrolyte uptake} = (W_1 - W_2/W_2) \times 100 \quad (1)$$

where W_2 and W_1 show the weight of the fresh and soaked polymeric films, respectively. Also, the flammability test of G-SPE_TMSP (1–5 wt%) was carried out to understand thermal stability.

Theoretical calculations

Gaussian 9 software was used for the density functional theory (DFT) calculations. The calculations were carried out using a 6-31G basis set with the B3LYP functional. For NBO analysis, the 6-31G basis set was used with the cc-PVDZ functional. The HOMO–LUMO energy gap of the electrolyte components was calculated from the ΔE value given by ($\Delta E = E_{HOMO} - E_{LUMO}$). Now, for the NBO analysis, the higher the value of stabilization energy (E_2), the stronger the interaction between TMSP and F^-. Also, the lower the value of ΔE ($\Delta E = E_2 - E_i$), the stronger the interaction between TMSP and F^-.

Results and discussion

Material characterization

The X-ray diffraction analysis has been performed to understand the phase and structure of NMA (Fig. 1a) and the SPE film (Fig. 1b). The peaks at a 2θ value of 27.6° indicate the (002) crystal plane corresponding to BN present in the film, while those at 2θ values of 18.8° and 20.3° correspond to (100) and (020) crystal planes of the PVDF-HFP polymer matrix. Also, the XRD spectral analysis of NMA exhibits characteristic intense peaks corresponding to (003), (104), and (018) crystal planes, showing the formation of a phase pure NMA lattice. The FT-IR spectral analysis (Fig. 1c) of the G-SPE_B-EL and G-SPE_TMSP (1–5 wt%) has been carried out to determine the functionalities present in the electrolyte. The IR spectra corresponding to G-SPE_B-EL exhibit transmission peaks at 1392, 1455, 1482, and 1554 cm^{-1} corresponding to the asymmetric vibrations of C–O, C–H, C–C, and C=O functionalities, respectively, of EC, DMC, and PEC in the electrolyte. In addition, the presence of PEC formed by the polymerization of EC by AIBN has been elucidated from the spectral lines (Fig. S1†) corresponding to the out-of-plane bending mode of O–C–O–O (859 cm^{-1}), C–O–C (1099 cm^{-1}), O–C–O (1189 cm^{-1}), C=O (1760 cm^{-1}), and alkyl asymmetric and symmetric stretching (2935 and 3004 cm^{-1}) in the G-SPE_B-EL. The characteristic peaks corresponding to 970 and 1280 cm^{-1} corresponds to the P–O and P=O functionalities of the TMSP additive. Further the peaks at 841 and 1072 cm^{-1}

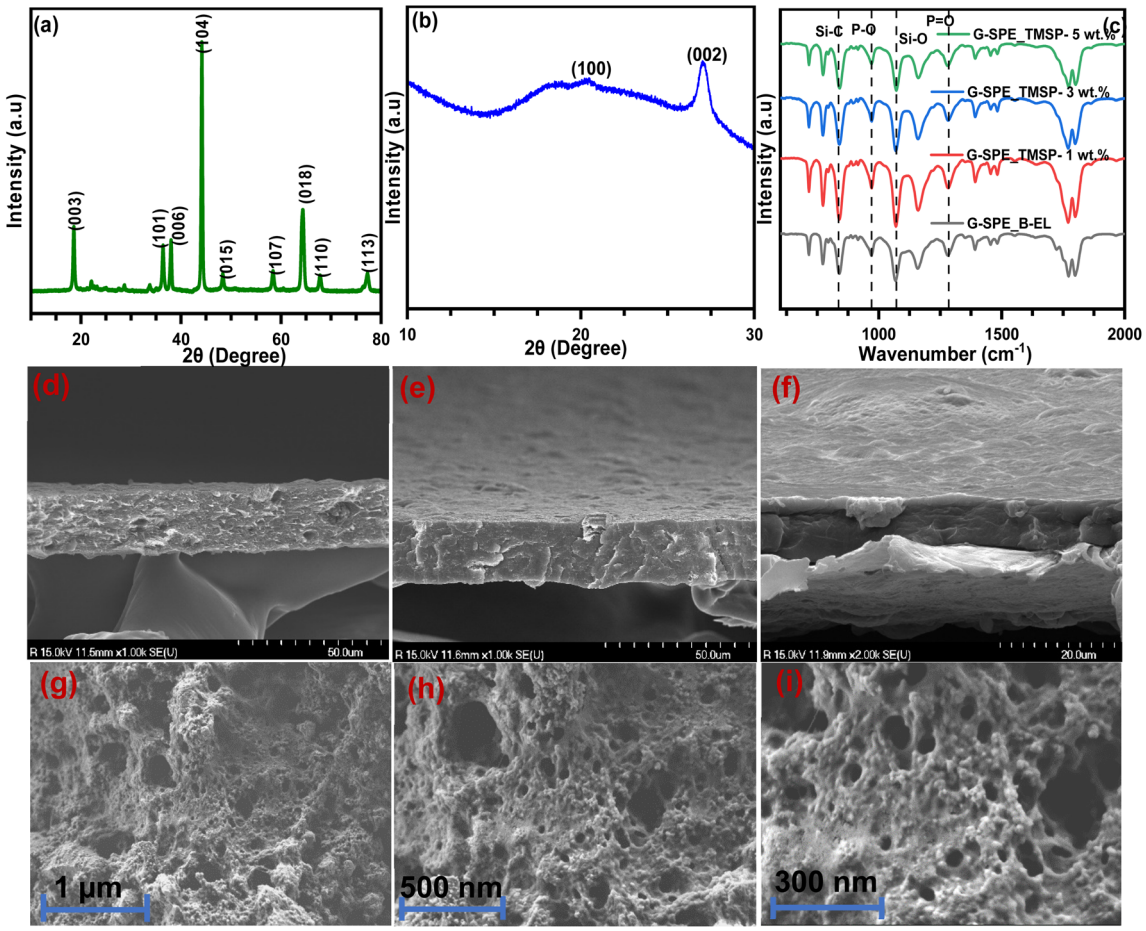

Fig. 1 XRD analysis of (a) NMA and (b) G-SPE, (c) IR spectrum of G-SPE_TMSP: 1–5 wt%, (d–f) FE-SEM cross-sectional images of G-SPE_TMSP: 1–5 wt% at (d, e) 50 μm and (f) 20 μm, and (g–i) FE-SEM images of the NMA cathode at (g) 1 μm, (h) 500 nm, and (i) 300 nm.

are attributed to the Si–C and Si–O components of TMSP, respectively. To further confirm the formation of PEC from EC, an *ex situ* polymerization reaction of EC into PEC in the presence of AIBN has been carried out, and the NMR spectra of the same have been recorded and compared with the results in ref. 32. The ^{1}H-NMR spectra of PEC show three different signals corresponding to protons a, b, c, and d. The intense peak at a chemical shift value of 3.5 ppm and the less intense peak at 3.7 ppm correspond to the methylene protons CH_2-c and CH_2-b adjacent to the ethereal linkage of PEC. Also, the less intense peak at 4.1 ppm corresponds to the methylene group, CH_2-a, adjacent to the ester moiety in the PEC. All these peaks correlate with the formation of PEC. However, an intense peak at 4.5 ppm corresponding to methylene protons of the CH_2-d in EC can still be observed in PEC, which further shows that some of the EC still remains in the mixture and is yet to get polymerized. In addition, on comparing the ^{1}H-NMR spectra of EC and PEC (Fig. S2a and b†), it can be clearly observed that the peak corresponding to methylene protons CH_2-a, CH_2-b, and CH_2-c of PEC grows as the reaction continues, while these peaks are absent in EC. Thus, the conversion of EC to PEC occurs as the reaction progresses. The ^{13}C-NMR spectra (Fig. S3a and b†) show the type of carbon moieties present in the compound. The high downfield peak at 155 ppm corresponds to the carbonate functionality of both EC and PEC. The peaks at the chemical shift values of 68.2 and 67 ppm correspond to the carbon atom adjacent to the carbonate group, while the downfield peaks at chemical shift values of 70, 72.4, and 74.5 correspond to the carbon atoms of the methylene groups adjacent to the ether functionalities. The presence of these ethereal linkages correlates with the observation from the IR spectra with the formation of O–C–O–O, C–O–C, and O–C–O functionalities, which also confirms the ring opening polymerization of EC by AIBN. The presence of these ethereal and carbonate linkages correlates with these mechanisms. Similar to the ^{1}H-NMR spectrum, the ^{13}C-NMR spectrum of PEC also exhibits a peak corresponding to EC at 65 ppm. As the reaction progresses, the peak corresponding to EC diminishes with an enhancement in the peak intensity of PEC's ethereal and carbonyl carbon atom peaks. In addition, the reaction mechanism involving the polymerization of EC into PEC is a type of radical-assisted ring-opening polymerization. In addition, the reaction mechanism involving the polymerization of EC into PEC is a type of radical-assisted ring-opening polymerization. The FE-SEM images (Fig. 1d–i) show the porous nature of the G-SPE film, hence improving the infiltration of the liquid electrolyte. In addition,

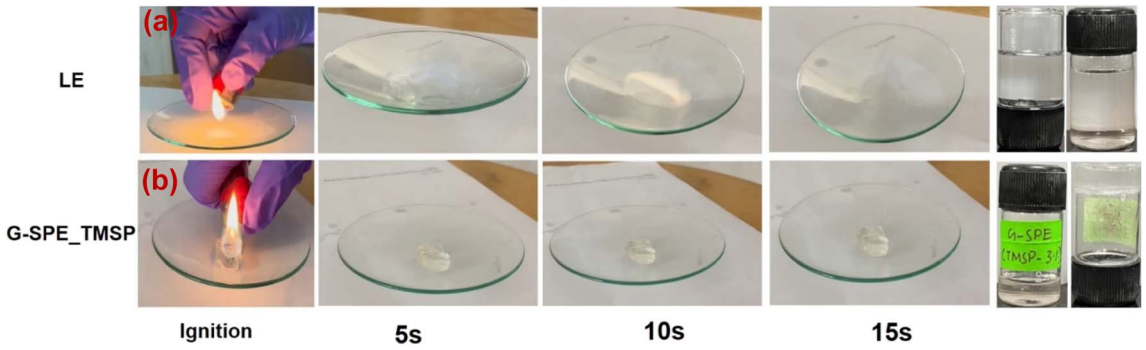

Fig. 2 Flammability test of (a) LE and (b) G-SPE_TMSP-3 wt%.

the porous nature can also be observed in the morphology of the NMA cathode, which enhances the Li-ion conduction during the charge–discharge process.

The electrolyte infiltration into the film plays a major role in providing a stable gel interface. The amount of electrolyte uptake by the film has to be quantified. The as-determined values of the electrolyte uptake by the film for TMSP: 1, 3, and 5 wt% are 65, 74, and 80%, respectively. In addition, the flammability test for G-SPE_TMSP: 1 wt% (Fig. S4 and S5†), G-SPE_TMSP: 3 wt% (Fig. 2), and G-SPE_TMSP: 5 wt% (Fig. S4†) exhibits better flame-retardant behavior even after igniting for a longer duration of 15 s. In contrast, liquid electrolytes (LEs) show poor fire retardancy and will catch fire easily. However, the flammability test for the LE containing TMSP (Fig. 2) shows that as the amount of TMSP increases from 1 to 5 wt%, the electrolyte's fire-retardant nature increases. This shows the fire-retardant nature of TMSP, and the flame will persist for a duration of 10 s in the case of TMSP-5 wt%.

Theoretical studies of G-SPE_TMSP

The neighboring bond orbital (NBO) calculations have been carried out to quantify the interactions between the TMSP and F^- ions. From the NBO study, it is evident that the F acts as a donor and will donate the lone pair (LP) and core–shell (CR) electrons, while the P and Si atoms in TMSP act as an electron acceptor and will accept electrons to the anti-bonding σ*-orbital. From Table T1,† it can be observed that there is a stable interaction between the LP of F with the σ*-orbitals of P and Si, as indicated by an enhancement in the magnitude of delocalization energy (E_2) to 10.41, 6.07, 7.29, and 3.49 kcal mol^{-1}, respectively, for the interaction between the LP of F and the σ*-orbitals of P 1–O 40, P 1–O 39, C 27–Si 42, and C 35–Si 42. On the other hand, a deterioration in the magnitude of E_2 to 1.01 kcal mol^{-1} can be observed for the interaction between the CR of F and the σ*-orbital of P 1–O 40. This strong interaction between the F and TMSP indicates the tendency of TMSP to scavenge the F^- ions. In addition, the energy level diagram (Fig. 3) shows a higher magnitude of ΔE for bare TMSP (−5.14 eV), while a lowering of the magnitude of ΔE has been observed in the case of TMSP-F (−3.82 eV), showing an increase in the stability of TMSP-F compared to TMSP, which further indicates the strong affinity of TMSP for F. The charge distribution during the TMSP–F interaction has been illustrated by the electrostatic potential (ESP) mapping (Fig. S6†), which shows a neutral

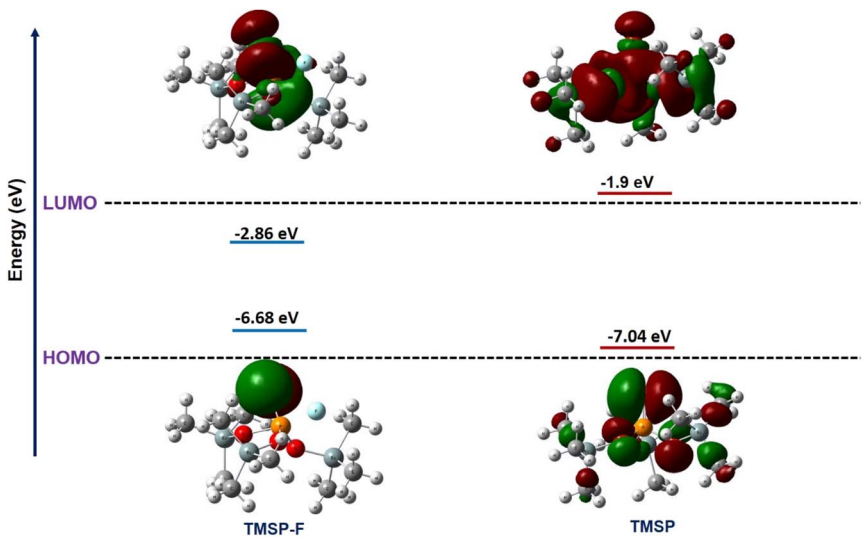

Fig. 3 The HOMO–LUMO energy levels of TMSP-F and TMSP.

charge region occupied by Si, C, and H, whereas the red region occupied by O, P, and F indicates the negatively charged region.

A comparison of energy of the highest occupied molecular orbital (HOMO) and the lowest unoccupied molecular orbital (LUMO) for different electrolyte components has been shown in Fig. S7.† The HOMO–LUMO energy level diagram illustrates the stability of the electrolytes, where a higher energy LUMO indicates higher reduction stability and a lower energy HOMO indicates higher oxidation stability. The magnitude of ΔE evaluated from the equation, $\Delta E = E_{HOMO} - E_{LUMO}$, also affects the electrolyte stability. The determined magnitude of ΔE for TMSP is −5.14 eV ($E_{HOMO} = -7.04$, $E_{LUMO} = -1.9$), EC is −6.21 eV ($E_{HOMO} = -7.3$, $E_{LUMO} = -1.09$), and DMC is −6.2 eV ($E_{HOMO} = -7.4$, $E_{LUMO} = -1.2$ eV). The HOMO level of TMSP is higher compared to those of electrolyte additives such as fluoroethylene carbonate (FEC) and solvents such as EC and DMC, hence indicating that TMSP owing to its low oxidation stability undergoes decomposition prior to other electrolyte components leading to the formation of a stable cathode electrolyte interface (CEI). Similarly, the lower energy LUMO of TMSP compared to FEC, EC, and DMC also enhances the initial decomposition of TMSP at the anodic side, forming a stable SEI at the anode. Hence, TMSP is a suitable electrolyte additive compared to additives such as FEC. Here, in the case of G-SPE_TMSP, the formation of an additional SEI or CEI layer by the decomposition of TMSP along with the gel will enhance the interfacial stability of the SE.

Electrochemical characterization of G-SPE_TMSP

The interfacial compatibility of the G-SPE with the Li-metal anode is a major factor determining the stability of the electrolyte, as poor interfacial compatibility results in non-uniform stripping/plating of Li-ions, leading to dendritic formation, causing short circuits (Fig. 4). The Li-ion diffusion through the G-SPEs has been investigated by determining the ionic conductivity and transference number (t_{Li^+}). The kinetics of Li-ions in the bulk are evaluated from the ionic conductivity of the Li-ions in the electrolytes. The ionic conductivity of G-SPE_TMSP (1–5 wt%) and G-SPE_B-EL has been determined from the electrochemical impedance spectroscopy (EIS) for the symmetric cell configuration of SS/G-SPE_TMSP (1–5 wt%)/SS and SS/G-SPE_B-EL/SS using the equation given by,

$$\sigma = L/R_b A \quad (2)$$

where R_b is the bulk resistance evaluated from the EIS plot, L is the thickness of the G-SPE (measured using a screw gauge), and A is the electrode–electrolyte contact area. The ionic conductivities examined from eqn (1) are of the magnitude of 2.48, 4.68, 7.14, and 8.57 mS cm^{-1}, for B-EL, TMSP: 1, 3, and 5 wt%, respectively. The calculated values of ionic conductivities are well within the range of the solid and gel-polymer-based electrolyte (10^{-3} to 10^{-4} mS cm^{-1}). The as-determined magnitudes of ionic-conductivities exhibit a trend that shows a proportional increase as the amount of TMSP increases from 1 to 5 wt%, while the magnitude of ionic conductivity is much lower among the G-SPE_B-EL. The poor ionic conductivity among the G-SPE_B-EL is due to the decomposition of the electrolyte, forming undesirable products in the bulk and causing sluggish Li-ion kinetics. On the other hand, in G-SPE_TMSP, the sacrificial decomposition of TMSP prevents further electrolyte decomposition in the bulk, thereby stabilizing the gel and enhancing the Li-ion kinetics compared to the G-SPE_B-EL. In addition, as the amount of TMSP is increased from 1 to 5 wt%, the decomposition of the electrolyte is further reduced, thereby enhancing the magnitude of ionic conductivity.

To further support this fact, the t_{Li^+} (Fig. 4a–d) has been evaluated from the symmetric cell, Li/G-SPE_TMSP (1–5 wt%)/Li, using the Bruce–Vincent equation given by,

$$t_{Li^+} = I^{ss}(\Delta V - I^0 R_i^0)/I^0(\Delta V - I^{ss} R_i^f) \quad (3)$$

where I^{ss} is the steady-state current, I^0 is the initial current, R_i^0 is the initial resistance, R_i^f is the final resistance, and ΔV is the voltage perturbation given. The as-determined magnitudes of t_{Li^+} are 0.70, 0.75, 0.79, and 0.83 for G-SPE_B-EL and G-SPE_TMSP (1–5 wt%), respectively. This similarity in the trend for both these parameters further shows the ion-conducting nature of the formed SEI layer.

To understand the influence of TMSP on the reaction kinetics, the activation energy (E_a) (Fig. 4e) has been determined from the Arrhenius plot. The evaluation of activation energy has been carried out from the $\ln(\sigma)$ *vs.* $1000/T$ plot by employing a symmetric cell with SS/G-SPE_TMSP (1–5 wt%)/SS configuration, using the equation given by,

$$\ln(\sigma) = \ln(\sigma_0) - E_a/1000RT \quad (4)$$

where σ is the ionic conductivity, σ_0 is the pre-exponential factor, E_a is the activation energy, and T is the temperature (in K, within the range of −10 to 100 °C). The E_a determined from eqn (3) shows the magnitudes of 0.42, 0.33, 0.25, and 0.13, respectively, for G-SPE_B-EL and G-SPE_TMSP: 1–5 wt%. The as-obtained trend of E_a can be ascribed to the enhancement of the Li-ion kinetics due to the formation of a stable and ion-conducting SEI layer as the amount of TMSP is increased from 1 to 5 wt%.

To examine the interfacial stability, the galvanostatic charge–discharge (GCD) study has been performed for a symmetric cell, Li/G-SPE_TMSP (1–5 wt%)/Li, at an aerial current density of 0.1 mA cm^{-2}. As can be observed from Fig. 4f–i, G-SPE_TMSP (1–5 wt%) exhibits stable cycling without any polarization for longer durations of 200, 500, and 2000 h, respectively, while the G-SPE_B-EL (where B-EL is the base electrolyte) exhibits a sudden voltage polarization during the initial duration and remains stable only up to 100 h. The stable stripping/plating behavior among the G-SPE_TMSP (1–5 wt%) can be ascribed to the formation of a stable SEI by TMSP along with the gel, which effectively prevents the dendritic formation due to homogeneous Li-ion deposition on the Li-metal anode. In contrast, the absence of an additional SEI layer along with the gel for the G-SPE_B-EL causes non-uniform Li stripping/plating, which eventually leads to dendritic growth. A solid proof for this statement can be obtained from the theoretical studies,

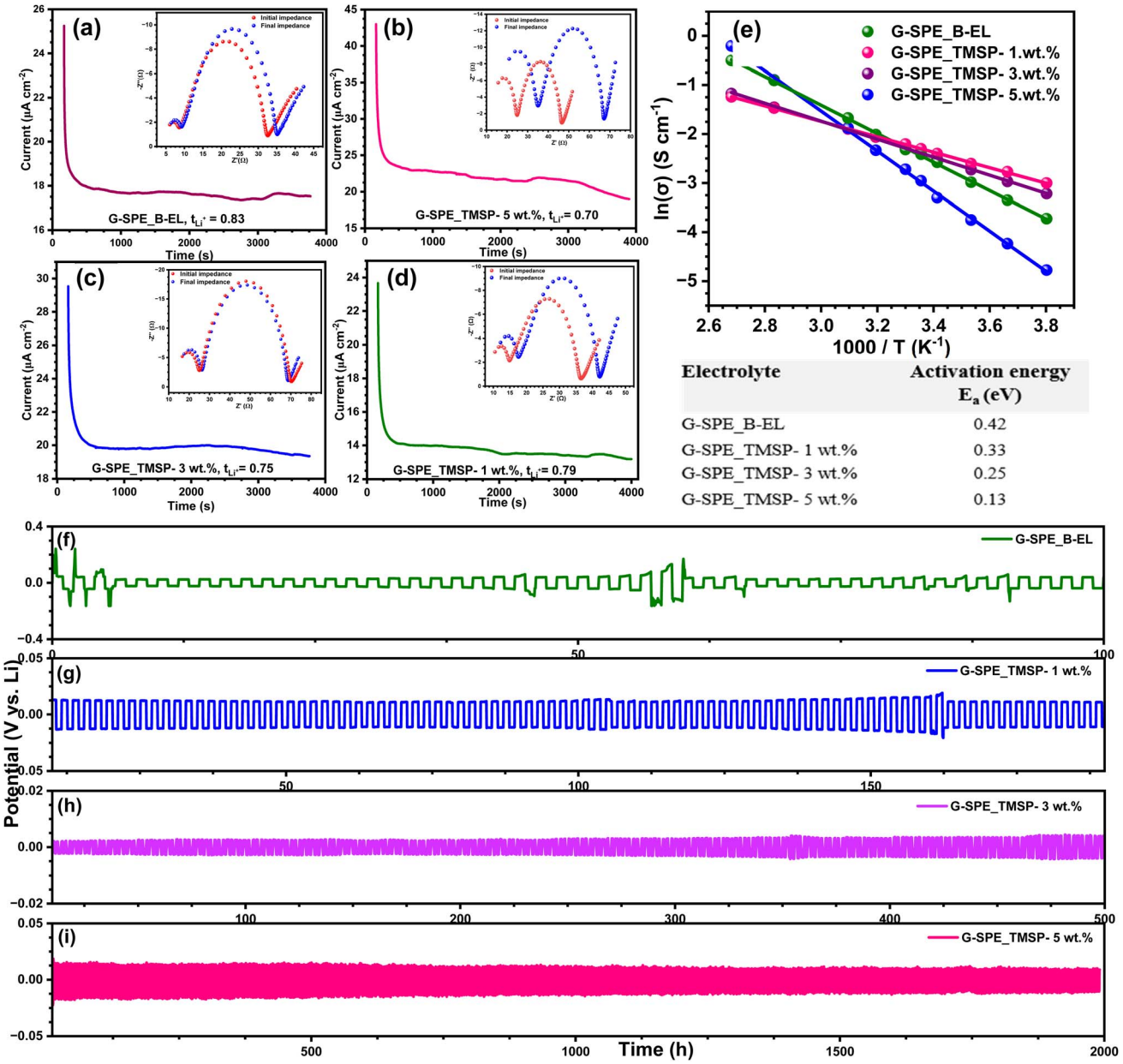

Electrolyte	Activation energy E_a (eV)
G-SPE_B-EL	0.42
G-SPE_TMSP- 1 wt.%	0.33
G-SPE_TMSP- 3 wt.%	0.25
G-SPE_TMSP- 5 wt.%	0.13

Fig. 4 Transference number calculation for (a) G-SPE_B-EL, (b) G-SPE_TMSP-5 wt%, (c) G-SPE_TMSP-3 wt%, and (d) G-SPE_TMSP-1 wt%. (e) Arrhenius plot for G-SPE_B-EL and G-SPE_TMSP (1–5 wt%). Stripping–destripping analysis of (f) G-SPE_B-EL, (g) G-SPE_TMSP-1 wt%, (h) G-SPE_TMSP-3 wt%, and (i) G-SPE_TMSP-5 wt% using symmetric cell analysis.

where the high energy HOMO (−7.04 eV) and low energy LUMO (−1.9 eV) of TMSP compared to other electrolyte components lead to poor oxidation stability, thereby undergoing oxidation prior to other electrolyte components forming a stable SEI layer with the gel (formed by the radical polymerization of EC by AIBN by thermal treatment). The as-formed SEI layer will enhance the electrolyte stability, and the stability increases as the concentration of TMSP is increased from 1 to 5 wt% due to the formation of a thicker SEI layer. Also, an experimental proof for SEI layer formation with the gel has been obtained from the EIS studies of the G-SPE_TMSP (1–5 wt%). Furthermore, TMSP also enhances the stability by enhancing the facile Li-ion conduction due to its F^- scavenging nature, preventing any side reactions with the electrolyte and forming a Li-ion conducting SEI layer. On the other hand, the G-SPE_B-EL electrolyte will undergo continuous decomposition, which enhances the parasitic side reactions and the growth of the SEI layer, thereby causing a drastic decrease in the Li-ion conduction and, hence, the electrolyte stability. In addition, the symmetric cell study of the electrolyte has been performed at a high areal current density of 1 mA cm^{-2} (Fig. S8†), which exhibits large polarization in the initial cycles, showing that the GCD cycling of the electrolyte can be carried out at a lower areal current density. Hence, to optimize the suitable aerial areal current density for the stable cycling of the electrolyte,

the symmetric cell study has been conducted at different areal current densities of 0.1, 0.5, and 1 mA cm^{-2}, as shown in Fig. S9,† among which 0.1 mA cm^{-2} exhibits less polarization up to 200 h, while 0.5 and 1 mA cm^{-2} show large polarization during the initial duration. Hence, the aerial current density for stable cycling has been optimized to be 0.1 mA cm^{-2}. In addition, the stability of the electrolyte has been further evaluated by carrying out an asymmetric cell study using Cu as a counter electrode instead of Li with configuration, Li/G-SPE_TMSP-3 wt%/Cu, at a current density of 0.1 mA cm^{-2} (Fig. S10†), and the cell exhibits better stability up to a duration of 270 h. Also, the coulombic efficiency (Fig. S11†) of Li/G-SPE_TMSP-3 wt%/Cu has been evaluated to be ~96% after 50 cycles. This observation opens up the possibility of G-SPE_TMSP being applied to anode-less solid-state batteries.

Electrochemical study of G-SPE_TMSP (1–5 wt%) with NMA

The electrochemical compatibility and the interfacial stability of the G-SPE_TMSP (1–5 wt%) in a practical LIB have been analyzed in a coin-cell setup using NMA as a cathode and a Li-metal anode denoted as NMA/G-SPE_TMSP (1–5 wt%)/Li within a potential window of 2.8–4.4 V *vs.* Li at a current density of 20 mA g^{-1}. The GCD profile (Fig. 5a and b) of NMA exhibits discharge capacities of 195, 202, and 199 mA h g^{-1} with a capacity retention of 79, 83, and 80% after 150 cycles when cycled in G-SPE_TMSP-1 wt%, G-SPE_TMSP-3 wt%, and G-SPE_TMSP-5 wt%, respectively. However, a decrement in capacity retention of 72% was observed for NMA cycled with the G-SPE_B-EL. This observation suggests the formation of a stable CEI layer in the presence of TMSP along with the as-formed gel. Moreover, due to its Lewis acidic nature, the Si atom in the TMSP acts as an F^- ion scavenger, hampering the parasitic side reactions initiated by the F^- ions. This observation can be proved by the HOMO–LUMO analysis and the NBO analysis of TMSP and TMSP-F. From the HOMO–LUMO calculations, it is evident that the formation of TMSP-F is thermodynamically more favorable, hence making the interaction of TMSP with F^- stronger, which makes TMSP a potential F^- scavenger. Also, the NBO analysis further shows a low ΔE value for the interaction between F^- and Si atoms in TMSP, agreeing that TMSP can act as a potential F^- scavenger. Also, an enhancement in capacity retention can be observed as the TMSP concentration is increased from 1 to 3 wt% due to an increase in the stability of the CEI layer, while the slight deterioration in the capacity retention as the TMSP concentration is increased to 5 wt% is due to the increase in the thickness of the CEI layer. This increase in thickness can be explained by the CEI formation mechanism by TMSP.[33] In this mechanism, the CEI is formed by a radical pathway, whereas in the initial step, TMSP undergoes radical cleavage, forming a TMSP radical, which will react further with other TMSP molecules forming trimethylsilane, which is one of the major components of the CEI layer. In the case of 1 to 3 wt% of TMSP, this reaction forming the trimethylsilane will cease within the initial stage of the reaction due to the limited amount of TMSP. In contrast, for 5 wt% of TMSP, even after forming the CEI layer by TMSP, its relatively large amount will further initiate a chain reaction, forming a large amount of trimethyl silane, which eventually increases the thickness of the CEI layer. In addition, the TMSP radical can also reduce other organic components within the electrolyte, particularly unpolymerized EC, DMC, *etc.*, whose reduction results in the formation of organic by-products that can increase the thickness of the CEI layer. Groher *et al.*[33] proved this mechanism using the XPS analysis conducted on the NMC811 electrode cycled in the TMSP electrolyte, where they observed a P–O functional peak in the XPS spectra at a lower TMSP concentration, while this peak diminishes as the TMSP concentration is increased to 5 wt% due to the deposition of more trimethyl silane and other organic by-products on the already existing CEI layer formed by TMSP. In addition, they reported a dramatic decrease in the electrochemical performance in NMC811 cycled in 5 wt% TMSP due to a proportional increase in the thickness of the CEI layer. Hence, this mechanism further depicts the increase in thickness of the CEI layer with a proportional increase in the wt% of TMSP. The GCD profile of NMA cycled in G-SPE_TMSP-5 wt% and LE_TMSP-5 wt% further shows that there is an enhancement in the cycle stability of the former compared to the latter. Also, the capacity retention of NMA cycled in G-SPE_TMSP-5 wt% is evaluated to be ~85%, while that cycled in LE_TMSP-5 wt% is ~63% after 100 cycles. This enhancement in the electrochemical performance of NMA cycled in the gel electrolyte can be attributed to the formation of a stable gel with the CEI layer in the case of G-SPE_TMSP-5 wt%. On the other hand, in LE_TMSP-5 wt%, a stable CEI layer has been formed; the poor oxidative stability of the liquid electrolyte components, such as EC and DMC, causes further electrolyte decomposition, leading to poor electrochemical stability. Hence, this shows that the physical state of the electrolyte plays a crucial role in determining the electrolyte stability. This observation can be clarified from the linear sweep voltammetry (LSV) plot of liquid and gel electrolytes, where the gel exhibits better oxidative stability than the liquid electrolyte (Fig. S12†). In addition, the GCD study of NMA has been carried out at a higher current density of 100 mA g^{-1} (Fig. S13†), which exhibits poor discharge capacity and cycle stability. To optimize the current density for the facile cycling of the cell, the rate performance study (Fig. 5d) has been performed at current densities from 20 to 200 mA g^{-1}, which exhibits capacity retentions of 80, 87, and 82% for G-SPE_TMSP-1 wt%, G-SPE_TMSP-3 wt%, and G-SPE_TMSP-5 wt%, respectively, which depicts the effectiveness of the as-formed CEI layer with the gel. Also, the TMSP concentration for effective CEI layer formation with G-SPE has been optimized to be 3–5 wt%. To further illustrate the wide applicability of the optimized electrolyte, electrochemical studies of G-SPE_TMSP: 3 wt% have been carried out with a commercial spinel-based $LiNi_{0.5}Mn_{1.5}O_4$ (LNMO) high voltage cathode within a potential window of 3–5 V (*vs.* Li) at a current density of 50 mA g^{-1}. The GCD studies (Fig. S14†) of the cycled LNMO exhibit an initial discharge capacity of 134 mA h g^{-1} with excellent capacity retention of 90% after 100 cycles. Hence, the use of the above electrolyte combination in high-voltage cathodes further elaborates its

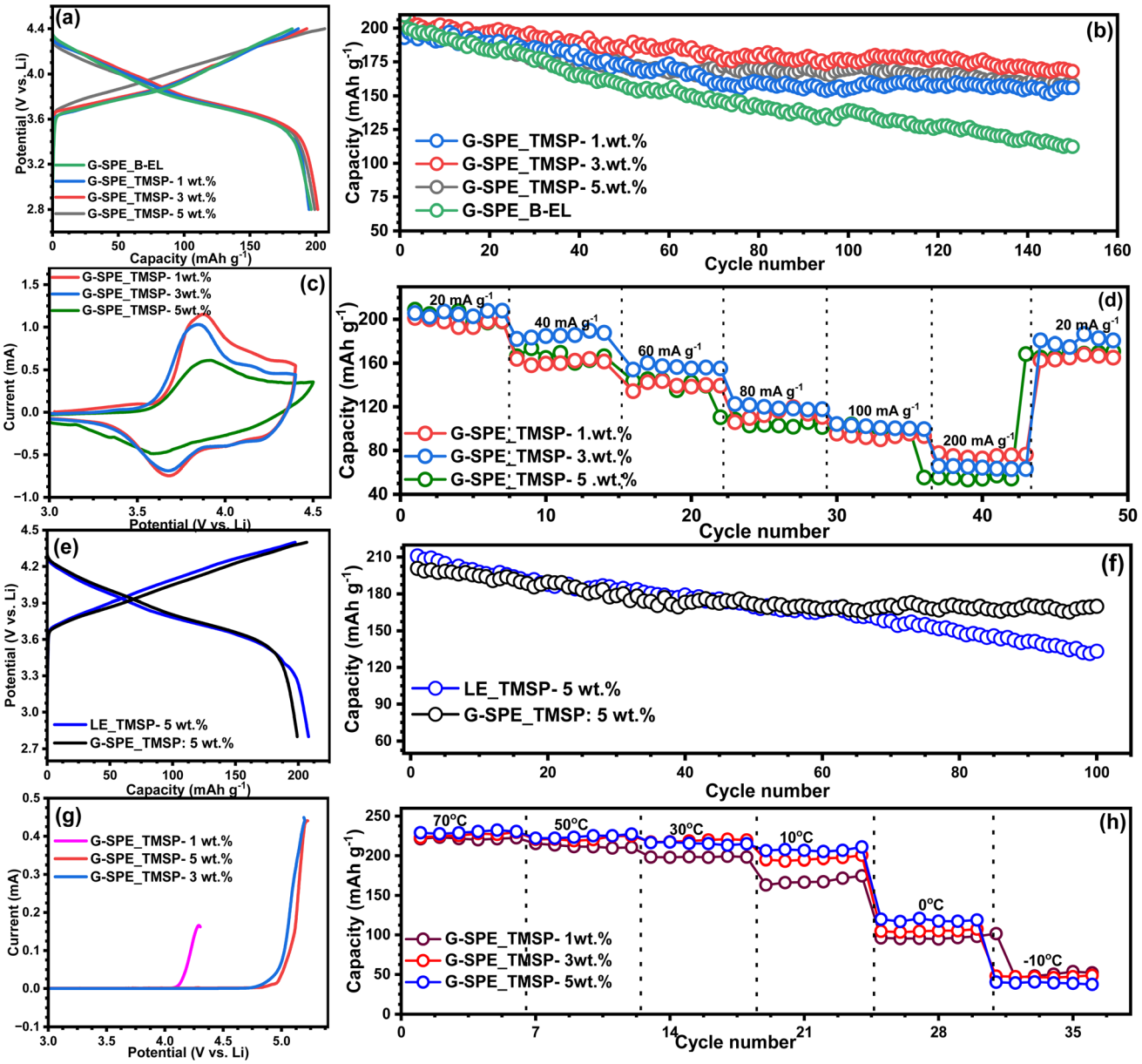

Fig. 5 (a and b) GCD plots of NMA with G-SPE_TMSP (1–5 wt%), (c) CV of NMA with G-SPE_TMSP (1–5 wt%) at a scan rate of 0.1 mV s^{-1}, (d) rate performance profile of NMA with G-SPE_TMSP (1–5 wt%), (e and f) GCD plots of NMA in LE_TMSP-5 wt% and G-SPE_TMSP-5 wt%, (g) LSV profile of G-SPE_TMSP (1–5 wt%), and (h) temperature study of NMA with G-SPE_TMSP (1–5 wt%) at temperatures from −10 to 70 °C.

wide stability range, making it applicable to both low- and high-voltage cathodes.

To understand the practical suitability at different climatic conditions, the electrochemical performance of NMA/G-SPE_TMSP (1–5 wt%)/Li has been performed at different temperatures ranging from −10 to 75 °C. The GCD plot (Fig. 5h) shows that at moderate and high temperatures, the NMA/G-SPE_TMSP (1–5 wt%)/Li exhibits excellent electrochemical performance, which can be attributed to the fast Li-ion kinetics due to thermal agitation. In contrast, a deterioration in the electrochemical performance can be observed as the temperature is lowered to 0 and −10 °C due to sluggish Li-ion kinetics. Apart from the sluggish Li-ion kinetics, the increase in viscosity at low temperatures leads to the solidification of the gel–polymer interface due to the presence of a high freezing point of EC forming the PEC (freezing point of EC is 36.4 °C), causing poor electrochemical performance and battery failure.[34] Furthermore, the increase in polarization at low temperatures can also contribute to poor electrochemical performance. Also, the interaction between the Li-ions and the electrolyte solvents becomes more pronounced at low temperatures, which also leads to poor Li-ion kinetics. However, the structural stability of the electrodes is still maintained at low temperatures, showing that no phase change has happened in this condition.

The cyclic voltammetry (CV) analysis (Fig. 5c) of NMA with G-SPE_TMSP (1–5 wt%) has been carried out at a scan rate of 0.1 mV s^{-1}. The CV curves show an oxidation and a reduction peak corresponding to Mn redox couples at 4 and 3.6 V *vs.* Li,

respectively. Also, a fall in the oxidation and reduction peak current can be observed as the TMSP concentration is increased from 1 to 5 wt% due to an increase in the thickness of the CEI layer. Moreover, the redox peaks become less prominent as the amount of TMSP increases. LSV has been performed to analyze the stability of the electrolytes (Fig. 5g). The LSV plot exhibits an increase in oxidation stability as the TMSP concentration is increased from 1 to 5 wt%. This can be attributed to the increase in the stability of the as-formed CEI layer, preventing electrolyte decomposition. In addition, LSV analysis of G-SPE_B-EL and LE (Fig. S10†) shows better oxidation stability for the G-SPE_B-EL, hence showing that the state of the electrolyte, whether gel or liquid, also contributes to the enhancement in the electrolyte stability.

The Li-ion kinetics for the G-SPE_TMSP (1–5 wt%) has been investigated using the electrochemical impedance spectroscopy (EIS) (Fig. 6) technique performed within a frequency range of 10 kHz to 0.1 Hz. The EIS profile of G-SPE_TMSP (1–5 wt%) exhibits an initial rise in the R_{CT} value, which can be attributed to the formation of the CEI layer by TMSP. However, a decrease in the R_{CT} value can be observed as the cycling progresses to the 10th cycle due to the formation of a stable CEI layer. Also, as the cycling advances towards the 50th and 100th cycles, the R_{CT} remains stable and does not show any rise, which further depicts that the as-formed CEI–gel interface is stable and prevents the electrolyte decomposition. In addition, the equivalent circuit corresponding to the EIS plot exhibits circuit elements corresponding to solution resistance (R_s), resistance due to the CEI layer and gel interface (R_{CT}), capacitive parts exhibiting the double-layer capacitance offered by the CEI and gel at the high-frequency region (Q_1 and Q_2, respectively) and a rising Warburg (Z_W) tail indicating that the mass-transfer

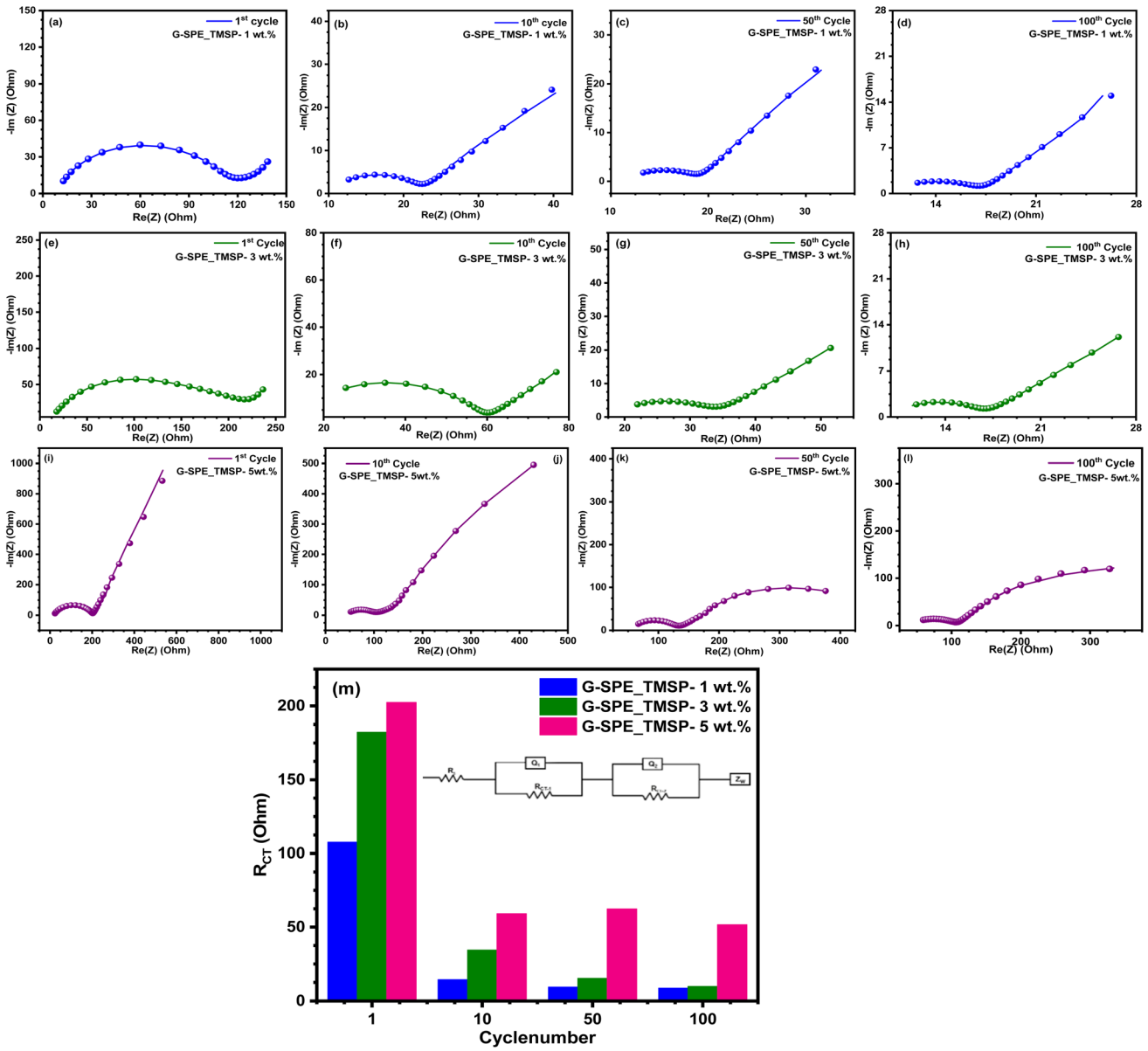

Fig. 6 (a–l) EIS profiles and (m) R_{CT} *vs.* cycle number graph of G-SPE_TMSP (1–5 wt%).

resistance can be observed in the low-frequency region. The fitting parameters of the Nyquist plot for the 1st cycle are given in Table T4.†

The *in operando* XRD analysis has been carried out to understand the phase transition accompanying the charge–discharge of NMA within a potential window of 2–4.4 V (Fig. 7). From the XRD spectra, the diffraction peaks corresponding to (333), (101), (006), (104), (015), (018), and (110) crystal planes can be observed at 2θ values of 19.8°, 38.7°, 39.2°, 45.3°, 45.7°, 65.5°, and 65.9°, respectively. Among the XRD spectra of different crystal planes, the (101), (006), (104), (015), (018), and (110) crystal planes show a slight peak shift, while the (003) crystal plane exhibits a significant peak shift. As the charging progresses to 4.15 V *vs.* Li, a significant positive shift in the (003) diffraction peak by ~0.02° (2θ: 19.5 to 19.52) can be observed, which can be attributed to a monoclinic (M) to hexagonal (H) phase shift. At 4.3 V *vs.* Li, a peak shift of ~0.08° can be observed, which signifies a phase change from the monoclinic (M) to the hexagonal (H_2) phase. Furthermore, as the charging progresses to a higher potential of 4.4 V, a more significant peak shift of ~0.1° can be observed due to a phase change from the hexagonal (H_2) to the hexagonal (H_3) phase. On the other hand, a negative shift peak shift can be observed in the case of discharge, and the shift becomes more negative at low operating potentials. The shift in the (003) crystal planes is closely correlated with the layered cathode materials, particularly NMC and NCA. In comparison with the previous reports on NMA based on liquid electrolytes, the *in operando* XRD imaging of the same exhibits a relatively large phase transition among the (003) and (104) crystal planes, while the phase transition has been confined within the (003) crystal plane on using the G-SPE as an electrolyte.[35] Although the phase transition of NMA is its intrinsic property, here, the study shows that the gel-polymer electrode–electrolyte interface, due to its relatively elastic nature, highly lowers the extent of phase transition in NMA, thereby improving its structural stability.[36–46] Also, the SEI layer formed by TMSP remains intact on the surface of the electrode due to the strong interaction between the NMA and the Si and P atoms present in TMSP, hence mitigating the phase change in the electrode to an extent. Furthermore, the Lewis acidic nature of the Si atom in the SEI layer prevents any nucleophilic attack by the F^- ions, thereby preventing electrode degradation and transition metal dissolution. Here, the TMSP alone is not effective in suppressing the phase change, but the synergetic effect of both the TMSP-derived SEI and gel–polymer interface has acted together to mitigate the phase change. The same is evident from the GCD study of NMA in the G-SPE and LE, wherein NMA cycled in the LE shows relatively poor cycle stability compared to that cycled in the G-SPE. In the future, this relatively new electrolyte configuration can be employed for various other layered cathode materials, particularly NMC and NCA.

Post-analysis of the G-SPE_TMSP (1–5 wt%) was performed using XRD, while FE-SEM was used to analyze the elemental

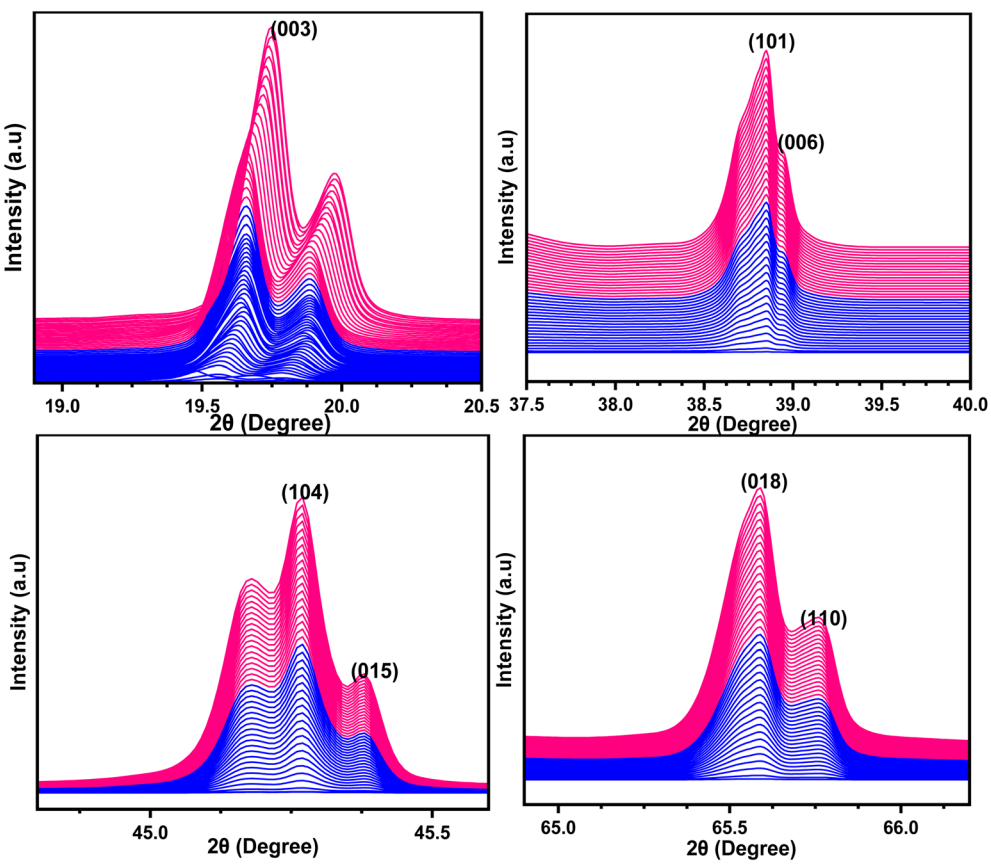

Fig. 7 *In operando* XRD analysis of NMA with G-SPE_TMSP-3 wt%.

distribution of the cycled NMA electrode (Fig. S15†) and G-SPE_TMSP (1–5 wt%) (Fig. S16†). The XRD spectra of both fresh and cycled G-SPE_TMSP (Fig. S17†) exhibit peaks at (002) and (100), corresponding to BN and PVDF-HFP of the SPE film. However, for the cycled G-SPE_TMSP, the peak at (002) becomes more prominent, which is attributed to the phase transition due to gelation. Moreover, the cycled G-SPE_TMSP exhibits additional diffraction peaks, indicating that the CEI layer formed along with the gel. The elemental distribution of the cycled G-SPE_TMSP and electrode has been analyzed using energy dispersion X-ray spectroscopy (EDS) analysis. The EDS analysis of the electrodes shows a slight decrease in the elemental distribution of Al, Mn, and Ni in cycled electrodes due to some sort of parasitic side reaction causing metal-ion dissolution. In addition, the EDS mapping of the G-SPE_TMSP electrolyte shows a low F content in the cycled electrolyte compared to the uncycled electrolyte. This can be ascribed to the strong coordination of the P and Si atoms in TMSP with the F^- anions, hence limiting the parasitic side reactions initiated by the F^- anions, leading to metal dissolution. In addition, the high O and P contents in the cycled G-SPE_TMSP compared to the uncycled one is due to the formation of the stable CEI film by TMSP with the gel. The surface elemental distribution of the cycled NMA electrode has been further evaluated using X-ray photoelectron spectroscopy (XPS) analysis. The XPS analysis (Fig. S18†) indicates the distribution of elements, such as Si, C, O, F, and Ni, in the electrode. The presence of Si on the electrode surface agrees with the formation of a CEI layer by TMSP along with the gel. Also, the F 1s spectra further indicate that the majority of the F^- ions are present on the electrode surface, which supports the F^--ion scavenging nature of the Si-rich CEI layer formed by the decomposition of TMSP at the electrode–electrolyte interface. In addition, Si binds with the F^- ions in the electrolyte, forming Me_3SiF, which has been observed in previous reports. The Ni 2p spectra corresponding to Ni $2p_{1/2}$ and Ni $2p_{3/2}$ show that the as-formed CEI layer with the gel prevents the dissolution of transition metals by mitigating the parasitic side reactions initiated by the F^- ions. Also, O 1s spectra corresponding to Ni–O (529 eV), C–O (531.5 eV), and C=O (532.8 eV) support the fact that the compound does not undergo any distortion or phase change even after cycling. In previous studies elucidating the mechanism of the TMSP electrolyte additive, the formation of Me_3SiF has been proved by various methods.[36] Similarly, here, from the XPS analysis, the decrease in the F^- ion composition and the presence of Si on the electrode surface further show the formation of Me_3SiF upon cycling. Also, the post-analysis study indicates the as-formed gel interface's stability and confirms the absence of any phase transition with the NMA. Moreover, using G-SPE_TMSP overcomes the electrolyte decomposition, which improves the cycle stability and coulombic efficiency and mitigates the parasitic side-reaction between the electrode and the electrolyte. In addition, on comparison of different electrochemical parameters such as ionic conductivity, transference number, and stability window, the present electrolyte system, G-SPE_TMSP, outperforms the previously reported gel-polymer electrolytes, the data of which are elaborated in Table T5.†

Conclusion

This study reveals the influence of a film-forming electrolyte additive, TMSP, in enhancing the electrochemical stability of a gel-solid polymer electrolyte (G-SPE) by varying its concentration from 1 to 5 wt%. The electrochemical stability of the electrolyte was analyzed using a symmetric cell arrangement, which indicates an enhancement in the electrolyte stability as the concentration of TMSP was increased from 1 to 5 wt% due to the formation of a stable SEI layer along with the gel. Also, the ionic conductivity of the electrolyte exhibits magnitude in the order of $\sim 10^{-3}$ S cm^{-1}, while it exhibits an increase in magnitude as the TMSP concentration was increased from 1 to 5 wt%. Similarly, the t_{Li^+} exhibits a similar trend with magnitudes ranging from 0.70 to 0.83 for TMSP within 1 to 5 wt%. In addition, the E_a calculated from the Arrhenius plot exhibits an increase in their magnitude for TMSP from 1 to 5 wt%, which is in close correlation with the as-determined magnitudes of ionic conductivity and t_{Li^+}. Also, the practical utility of the G-SPE_TMSP was analyzed from the GCD studies with the NMA cathode and Li metal anode. The GCD profile indicates an enhancement in the electrochemical performance of NMA in G-SPE_TMSP (1–5 wt%) compared to that in G-SPE_B-EL. In addition, capacity retention exhibits an increase in magnitude as the TMSP concentration increases from 1 to 5 wt% due to the increase in stability of the formed CEI layer. The *in operando* analysis shows the absence of any phase transition during charge–discharge. In addition, the post-analysis of the G-SPE_TMSP and NMA electrode further reveals the absence of any parasitic side reactions between the electrode and the electrolyte. Future research on LIBs is mainly focused on the development of SPEs. The research on gel SPEs has to be focused on developing novel polymer matrices based on PEO, PMMA, PAN, *etc.*, and also on developing novel polymer fillers such as BN, SiO_2, Al_2O_3, *etc.* Moreover, strategies must be employed to improve the interfacial electrode–electrolyte contact and mitigate the interfacial resistance, which should be prioritized.

Data availability

The data supporting this article have been included as part of the ESI.†

Conflicts of interest

There are no conflicts to declare.

Acknowledgements

SS acknowledges the Council of Scientific and Industrial Research (CSIR), Govt. of India, for the fellowship. YSL acknowledges the financial support from the National Research Foundation of Korea (NRF) grant funded by the Korean government (Ministry of Science, ICT & Future Planning) (No. RS-2023-00208361). VA acknowledges financial support from the Anusandhan National Research Foundation (ANRF), Govt. of India, through the Swarnajayanti Fellowship (SB/SJF/2020-21/12).

References

1 Z. Zhang, T. Ding, Q. Zhou, Y. Sun, M. Qu, Z. Zeng, Y. Ju, L. Li, K. Wang and F. Chi, A Review of Technologies and Applications on Versatile Energy Storage Systems, *Renew. Sustain. Energy Rev.*, 2021, **148**, 111263, DOI: 10.1016/j.rser.2021.111263.

2 S. Sreekumar, S. Natarajan and V. Aravindan, Recent Advancements in $LiCoPO_4$ Cathodes Using Electrolyte Additives, *Curr. Opin. Electrochem.*, 2021, **31**, 100868, DOI: 10.1016/j.coelec.2021.100868.

3 D. J. Wuebbles and A. K. Jain, Concerns about Climate Change and the Role of Fossil Fuel Use, *Fuel Process. Technol.*, 2001, **71**(1), 99–119, DOI: 10.1016/S0378-3820(01)00139-4.

4 T. A. Carleton and S. M. Hsiang, Social and Economic Impacts of Climate, *Science*, 2016, **353**(6304), aad9837, DOI: 10.1126/science.aad9837.

5 G. A. Florides and P. Christodoulides, Global Warming and Carbon Dioxide through Sciences, *Environ. Int.*, 2009, **35**(2), 390–401, DOI: 10.1016/j.envint.2008.07.007.

6 A. Manthiram, A Reflection on Lithium–Ion Battery Cathode Chemistry, *Nat. Commun.*, 2020, **11**(1), 1550, DOI: 10.1038/s41467-020-15355-0.

7 A. Manthiram, An Outlook on Lithium Ion Battery Technology, *ACS Cent. Sci.*, 2017, **3**(10), 1063–1069, DOI: 10.1021/acscentsci.7b00288.

8 X. Yu, W. A. Yu and A. Manthiram, Advances and Prospects of High-Voltage Spinel Cathodes for Lithium-Based Batteries, *Small Methods*, 2021, **5**(5), 2001196, DOI: 10.1002/smtd.202001196.

9 J. B. Goodenough and K.-S. Park, The Li-Ion Rechargeable Battery: A Perspective, *J. Am. Chem. Soc.*, 2013, **135**(4), 1167–1176, DOI: 10.1021/ja3091438.

10 J. B. Goodenough and Y. Kim, Challenges for Rechargeable Li Batteries, *Chem. Mater.*, 2010, **22**(3), 587–603, DOI: 10.1021/cm901452z.

11 D. Deng, Li-Ion Batteries: Basics, Progress, and Challenges, *Energy Sci. Eng.*, 2015, **3**(5), 385–418, DOI: 10.1002/ese3.95.

12 S. Sreedeep, S. Praneetha, Y.-S. Lee and V. Aravindan, Influence of Lithium Difluoro (Oxalato) Borate Additive on the Performance of $LiCoPO_4$–$LiFePO_4$ Solid-Solution by Carbothermal Reduction, *ChemElectroChem*, 2022, **9**(19), e202200815, DOI: 10.1002/celc.202200815.

13 S. Sreekumar, S. Natarajan, Y.-S. Lee and V. Aravindan, LiDFOB Induced Interphase for High Voltage $LiFe_{0.15}Co_{0.85}PO_4$@C Cathode by Solid-state Synthesis, *Energy Technol.*, 2022, **11**(1), 2200988, DOI: 10.1002/ente.202200988.

14 S. Sreekumar, S. Natarajan, Y.-S. Lee and V. Aravindan, Stabilizing the High Voltage $LiCoPO_4$ Cathode *via* Fe-Doping in the Gram-Scale Synthesis, *Electrochim. Acta*, 2022, **419**, 140367, DOI: 10.1016/j.electacta.2022.140367.

15 S. Sreedeep, Y.-S. Lee and V. Aravindan, Functional AlF3 Modification over 5.3 V Spinel $LiCoMnO_4$ Cathode for Li-Ion Batteries, *Composites, Part B*, 2024, 111365, DOI: 10.1016/j.compositesb.2024.111365.

16 S. Sreedeep, Y. S. Lee and V. Aravindan, Probing Enhanced Electrochemical Performance of Poly (3,4-Ethylenedioxy Thiophene) Encapsulated 5.3 V Spinel $LiCoMnO_4$ Cathode for Li-Ion Batteries, *Adv. Sustain. Syst.*, 2023, **7**(12), 2300267, DOI: 10.1002/adsu.202300267.

17 S. Sreedeep and V. Aravindan, Fabrication of 4.7 V Class "Rocking-Chair" Type Li-Ion Cells with Carbon-Coated $LiCoPO_4$ as Cathode and Graphite Anode, *Mater. Lett.*, 2021, **291**, 129609, DOI: 10.1016/j.matlet.2021.129609.

18 P. López-Aranguren, M. Reynaud, P. Głuchowski, A. Bustinza, M. Galceran, J. M. López Del Amo, M. Armand and M. Casas-Cabanas, Crystalline LiPON as a Bulk-Type Solid Electrolyte, *ACS Energy Lett.*, 2021, **6**(2), 445–450, DOI: 10.1021/acsenergylett.0c02336.

19 K. H. Park, K. Kaup, A. Assoud, Q. Zhang, X. Wu and L. F. Nazar, High-Voltage Superionic Halide Solid Electrolytes for All-Solid-State Li-Ion Batteries, *ACS Energy Lett.*, 2020, 533–539, DOI: 10.1021/acsenergylett.9b02599.

20 J. C. Barbosa, R. Gonçalves, C. M. Costa and S. Lanceros-Méndez, Toward Sustainable Solid Polymer Electrolytes for Lithium-Ion Batteries, *ACS Omega*, 2022, **7**(17), 14457–14464, DOI: 10.1021/acsomega.2c01926.

21 J. Mi, J. Ma, L. Chen, C. Lai, K. Yang, J. Biao, H. Xia, X. Song, W. Lv, G. Zhong and Y. B. He, Topology Crafting of Polyvinylidene Difluoride Electrolyte Creates Ultra-Long Cycling High-Voltage Lithium Metal Solid-State Batteries, *Energy Storage Mater*, 2022, **48**, 375–383, DOI: 10.1016/j.ensm.2022.02.048.

22 V. van Laack, F. Langer, A. Hartwig and K. Koschek, Succinonitrile-Polymer Composite Electrolytes for Li-Ion Solid-State Batteries – The Influence of Polymer Additives on Thermomechanical and Electrochemical Properties, *ACS Omega*, 2023, **8**(10), 9058–9066, DOI: 10.1021/acsomega.2c02174.

23 T. Wei, Z. Wang, Q. Zhang, Y. Zhou, C. Sun, M. Wang, Y. Liu, S. Wang, Z. Yu, X. Qiu, S. Xu and S. Qin, Metal-Organic Framework-Based Solid-State Electrolytes for All Solid-State Lithium Metal Batteries: A Review, *CrystEngComm*, 2022, **24**(28), 5014–5030, DOI: 10.1039/d2ce00663d.

24 M. Liu, S. Zhang, G. Li, C. Wang, B. Li, M. Li, Y. Wang, H. Ming, Y. Wen, J. Qiu, J. Chen and P. Zhao, A Cross-Linked Gel Polymer Electrolyte Employing Cellulose Acetate Matrix and Layered Boron Nitride Filler Prepared *via in Situ* Thermal Polymerization, *J. Power Sources*, 2021, **484**, 229235, DOI: 10.1016/j.jpowsour.2020.229235.

25 Z. Zhang, R. G. Antonio and K. L. Choy, Boron Nitride Enhanced Polymer/Salt Hybrid Electrolytes for All-Solid-State Lithium Ion Batteries, *J. Power Sources*, 2019, **435**, 226736, DOI: 10.1016/j.jpowsour.2019.226736.

26 G. Homann, L. Stolz, J. Nair, I. C. Laskovic, M. Winter and J. Kasnatscheew, Poly(Ethylene Oxide)-Based Electrolyte for Solid-State-Lithium–Batteries with High Voltage Positive Electrodes: Evaluating the Role of Electrolyte Oxidation in Rapid Cell Failure, *Sci. Rep.*, 2020, **10**(1), 4390, DOI: 10.1038/s41598-020-61373-9.

27 M. Yang, S. Li, G. Zhang, M. Huang, J. Duan, Y. Cui, B. Yue and H. Liu, $LiNO_3$-Assisted Succinonitrile-Based Solid-State Electrolyte for Long Cycle Life toward a Li-Metal Anode *via* an *In Situ* Thermal Polymerization Method, *ACS Appl. Mater. Interfaces*, 2023, **15**(14), 18323–18332, DOI: **10.1021/acsami.3c01134**.

28 J. Castillo, A. Santiago, X. Judez, I. Garbayo, J. A. Coca Clemente, M. C. Morant-Miñana, A. Villaverde, J. A. González-Marcos, H. Zhang, M. Armand and C. Li, Safe, Flexible, and High-Performing Gel-Polymer Electrolyte for Rechargeable Lithium Metal Batteries, *Chem. Mater.*, 2021, **33**(22), 8812–8821, DOI: **10.1021/acs.chemmater.1c02952**.

29 X. Zhao, C. Wang, H. Liu, Y. Liang and L.-Z. Fan, A Review of Polymer-Based Solid-State Electrolytes for Lithium–Metal Batteries: Structure, Kinetic, Interface Stability, and Application, *Batter. Supercaps*, 2023, **6**(4), e202200502, DOI: **10.1002/batt.202200502**.

30 G. Yan, X. Li, Z. Wang, H. Guo and C. Wang, Tris (Trimethylsilyl)Phosphate: A Film-Forming Additive for High Voltage Cathode Material in Lithium-Ion Batteries, *J. Power Sources*, 2014, **248**, 1306–1311, DOI: **10.1016/j.jpowsour.2013.10.037**.

31 Y. K. Han, J. Yoo and T. Yim, Why Is Tris (Trimethylsilyl) Phosphite Effective as an Additive for High-Voltage Lithium–Ion Batteries?, *J. Mater. Chem. A*, 2015, **3**(20), 10900–10909, DOI: **10.1039/c5ta01253h**.

32 R. Abdul-Karim, A. Hameed and M. I. Malik, Ring-Opening Polymerization of Ethylene Carbonate: Comprehensive Structural Elucidation by 1D & 2D-NMR Techniques, and Selectivity Analysis, *RSC Adv.*, 2017, **7**(19), 11786–11795, DOI: **10.1039/c7ra01113j**.

33 C. Groher, D. M. Cupid, Q. Jiang, E. Rosenberg and J. Kahr, Investigating the Multifunctional Role of Tris (Trimethylsilyl)Phosphite as an Electrolyte Additive *via* Operando Gas Chromatography/Mass Spectrometry and X-Ray Photoelectron Spectroscopy, *Adv. Energy Sustain. Res.*, 2025, 1–12, DOI: **10.1002/aesr.202400297**.

34 L. Luo, K. Chen, H. Chen, H. Li, R. Cao, X. Feng, W. Chen, Y. Fang and Y. Cao, Enabling Ultralow-Temperature (−70 °C) Lithium–Ion Batteries: Advanced Electrolytes Utilizing Weak-Solvation and Low-Viscosity Nitrile Cosolvent, *Adv. Mater.*, 2024, **36**(5), 1–9, DOI: **10.1002/adma.202308881**.

35 R. Essehli, A. Parejiya, N. Muralidharan, C. J. Jafta, R. Amin, M. B. Dixit, Y. Bai, J. Liu and I. Belharouak, Hydrothermal Synthesis of Co-Free NMA Cathodes for High Performance Li-Ion Batteries, *J. Power Sources*, 2022, **545**, 231938, DOI: **10.1016/j.jpowsour.2022.231938**.

36 A. Guéguen, C. Bolli, M. A. Mendez and E. J. Berg, Elucidating the Reactivity of Tris(Trimethylsilyl)Phosphite and Tris(Trimethylsilyl)Phosphate Additives in Carbonate Electrolytes – A Comparative Online Electrochemical Mass Spectrometry Study, *ACS Appl. Energy Mater.*, 2020, **3**(1), 290–299, DOI: **10.1021/acsaem.9b01551**.

37 Z. Zhang, G. Sui, H. Bi and X. Yang, Radiation-Crosslinked Nanofiber Membranes with Well-Designed Core–Shell Structure for High Performance of Gel Polymer Electrolytes, *J. Memb. Sci.*, 2015, **492**, 77–87, DOI: **10.1016/j.memsci.2015.05.040**.

38 M. R. Asghar, Y. Zhang, A. Wu, X. Yan, S. Shen, C. Ke and J. Zhang, Preparation of Microporous Cellulose/Poly(Vinylidene Fluoride-Hexafluoropropylene) Membrane for Lithium Ion Batteries by Phase Inversion Method, *J. Power Sources*, 2018, **379**, 197–205, DOI: **10.1016/j.jpowsour.2018.01.052**.

39 B. Liu, Y. Huang, H. Cao, L. Zhao, Y. Huang, A. Song, Y. Lin, X. Li and M. Wang, A Novel Porous Gel Polymer Electrolyte Based on Poly(Acrylonitrile-Polyhedral Oligomeric Silsesquioxane) with High Performances for Lithium-Ion Batteries, *J. Memb. Sci.*, 2018, **545**, 140–149, DOI: **10.1016/j.memsci.2017.09.077**.

40 S. Y. Xiao, Y. Q. Yang, M. X. Li, F. X. Wang, Z. Chang, Y. P. Wu and X. Liu, A Composite Membrane Based on a Biocompatible Cellulose as a Host of Gel Polymer Electrolyte for Lithium Ion Batteries, *J. Power Sources*, 2014, **270**, 53–58, DOI: **10.1016/j.jpowsour.2014.07.058**.

41 H. Bi, G. Sui and X. Yang, Studies on Polymer Nanofibre Membranes with Optimized Core–Shell Structure as Outstanding Performance Skeleton Materials in Gel Polymer Electrolytes, *J. Power Sources*, 2014, **267**, 309–315, DOI: **10.1016/j.jpowsour.2014.05.030**.

42 T. C. Nirmale, I. Karbhal, R. S. Kalubarme, M. V. Shelke, A. J. Varma and B. B. Kale, Facile Synthesis of Unique Cellulose Triacetate Based Flexible and High Performance Gel Polymer Electrolyte for Lithium Ion Batteries, *ACS Appl. Mater. Interfaces*, 2017, **9**(40), 34773–34782, DOI: **10.1021/acsami.7b07020**.

43 S.-D. Gong, Y. Huang, H.-J. Cao, Y.-H. Lin, Y. Li, S.-H. Tang, M.-S. Wang and X. Li, A Green and Environment-Friendly Gel Polymer Electrolyte with Higher Performances Based on the Natural Matrix of Lignin, *J. Power Sources*, 2016, **307**, 624–633, DOI: **10.1016/j.jpowsour.2016.01.030**.

44 B. Liu, Y. Huang, H. Cao, A. Song, Y. Lin, M. Wang and X. Li, A High-Performance and Environment-Friendly Gel Polymer Electrolyte for Lithium Ion Battery Based on Composited Lignin Membrane, *J. Solid State Electrochem.*, 2018, **22**(3), 807–816, DOI: **10.1007/s10008-017-3814-x**.

45 M. Zhu, J. Lan, C. Tan, G. Sui and X. Yang, Degradable Cellulose Acetate/Poly-l`Lactic Acid/Halloysite Nanotube Composite Nanofiber Membranes with Outstanding Performance for Gel Polymer Electrolytes, *J. Mater. Chem. A*, 2016, **4**(31), 12136–12143, DOI: **10.1039/c6ta05207j**.

46 M. Zhu, C. Tan, Q. Fang, L. Gao, G. Sui and X. Yang, High Performance and Biodegradable Skeleton Material Based on Soy Protein Isolate for Gel Polymer Electrolyte, *ACS Sustain. Chem. Eng.*, 2016, **4**(9), 4498–4505, DOI: **10.1021/acssuschemeng.6b01218**.